MARK A. BAKER, STEPHEN A. MACK, and DAVID P. VASHOLZ

OPTICAL PHASE FLUCTUATIONS IN THE OCEAN

Optical phase is central to the performance of ocean and laboratory measurement systems that rely on coherent optics. During the past several years, the Applied Physics Laboratory has conducted theoretical and laboratory investigations of the random fluctuations in optical phase that can be created by the temperature and salinity microstructure commonly found in the world's oceans.

INTRODUCTION

Highly sensitive measurements are required to observe and exploit many physical processes of great importance in oceanographic applications and research. Such measurements often involve small displacements or velocities such as the minute vibrations of fluid particles considered in ocean acoustics. Turbulence, which at its smallest scales converts the constantly replenished kinetic energy of the ocean into heat, is another ocean process frequently investigated. In addition, small movements of the ocean's interface with the atmosphere, the ice of the polar regions, or the ocean's bottom are of substantial interest.

Optical interferometric techniques have provided laboratory researchers for some time with highly sensitive means of measuring small displacements and related quantities. Perhaps the best-known example is the classical Michelson–Morely experiment, the results of which were later explained by special relativity. The development of the laser has greatly enhanced these techniques; a notable example of ongoing work is the Laser Interferometer Gravitational-Wave Observatory,[1] which will employ extremely sensitive interferometric techniques in an attempt to detect the gravitational waves generated by astronomical events.

Given the improvements in optical interferometric techniques, great interest is being expressed in the use of coherent underwater optical instruments and systems. By definition, the properties and integrity of the optical phase are crucial in determining the capabilities of such devices. Since one of the fundamental purposes of interferometers is to make remote measurements, one or more of the optical paths must travel directly through the ocean medium. When the instruments are towed through the water (and to a lesser degree when they are stationary), inhomogeneities in the index of refraction will be swept through the optical paths and will produce phase fluctuations. Depending on the instrument's application, the fluctuations may be regarded as signal or noise, but it is important to know or at least bound their overall magnitudes and scales. Two primary sources of refractive fluctuations are the temperature and salinity microstructure (scales on the order of meters down to millimeters) found throughout the world's oceans.

During the past few years, we have investigated the effects of optical phase fluctuations in a variety of contexts. Initial efforts focused on theoretical predictions of such effects as they might occur over typical ranges of oceanic parameters. Later work has emphasized the experimental confirmation of those predictions using the facilities of the APL Hydrodynamics Laboratory in a multidisciplinary effort involving wave propagation through a random medium, optics, oceanography, and turbulence. This article presents our results.

THEORY

For definiteness, we will restrict ourselves to a coherent optical system that makes remote fluid-velocity measurements: a reference beam laser-Doppler velocimeter (LDV). With an LDV, it is possible,[2] in principle, to measure the velocities of scattering particles in such a way that the system will respond only to particles that lie within a well-defined scattering volume some distance from the optical system. Such a system is shown schematically in Figure 1. Note that the scattering volume has been replaced with a mirror because our interest is not in the dynamics of the scatterers or in what takes place within the scattering volume but rather with what happens to the light as it passes to and from the scattering volume through the intervening ocean. If the mirror were to vibrate back and forth normal to its surface, the phase of the reflected light would vary proportionally to the

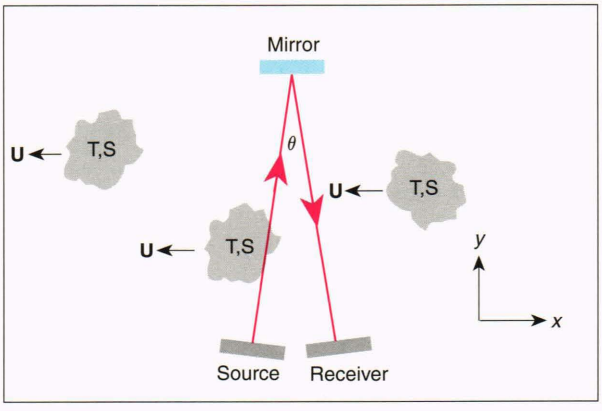

Figure 1. Rough schematic of a laser-Doppler velocimeter (LDV) system with scattering volume replaced by a mirror. The blobs represent naturally occurring temperature (T) and salinity (S) microstructure inhomogeneities and appear to move with some velocity **U** relative to the optical paths. Only the limit $\theta \rightarrow 0$ is considered.

mirror's displacement. This principle is also used to measure particle motion when a scattering volume is present. Any phase fluctuations generated by the ocean, however, will also be measured by the system and interpreted as particle motion even though the mirror (or scattering particles) is perfectly stationary. Hence, in this situation the index fluctuations caused by varying temperature and salinity are a source of noise masquerading as fluid velocities. Regions that differ in refractive index are also shown in Figure 1 as they are swept across the optical paths. The LDV will encounter such regions as it is towed through the ocean or if there is a mean current. In Figure 1, the motion of the inhomogeneities in optical refractive index is transverse to the optical path. This assumption is made throughout the article and has been adapted to other configurations by Vasholz, Baker, and Mack in a previous report,[3] hereafter designated VBM, which contains many of the detailed derivations of results given here.

Light Propagation in a Weakly Fluctuating Medium

The basic premise of the theory is that any given light wave will move so rapidly along its path that the optical properties of the water it encounters are virtually constant during its passage. The light wave will, however, pass through various regions of the water where the speed of light has slightly different values.

In a region where the refractive index is greater than its average value, the wave speed will be slightly less, as will the wavelength. Consequently, more wavelengths of light than usual will be required to traverse a given distance. The opposite will be true in regions where the index is smaller than its average value. This situation is shown graphically in Figure 2. If the index fluctuations are weak enough and the range is small enough, it can be shown that the amplitude of the light waves will be virtually unaffected.

With reference to Figure 1, the optical phase change experienced by a light ray in its round trip from transmitter to mirror and back to receiver is an integral along the optical path given by

$$\phi(x,z,t) = 2q\, n_0^{-1} \int_0^L dy\, n(x,y,z,t)\,, \qquad (1)$$

where q is the wave number (2π divided by the wavelength in water) in the absence of index fluctuations, L is the distance out to the mirror, n_0 is the mean index of refraction, and $n(x,y,z,t)$ is the fluctuating index of refraction field as a function of space and time. Note that, if there are no fluctuations, $\phi = 2qL$. As time advances, a new set of index fluctuations will lie along the optical path, the integrand in Equation 1 will be altered, and a different value will be obtained for the change in optical phase. It is this change in optical phase as a function of time that is of primary interest in our work. Suppose that the mirror is vibrating in a direction normal to its surface and parallel to the optical path but that there are no index fluctuations. Then, L is a function of time, and one can estimate the velocity v of the mirror in terms of the phase rate $\dot{\phi}$ with the relation

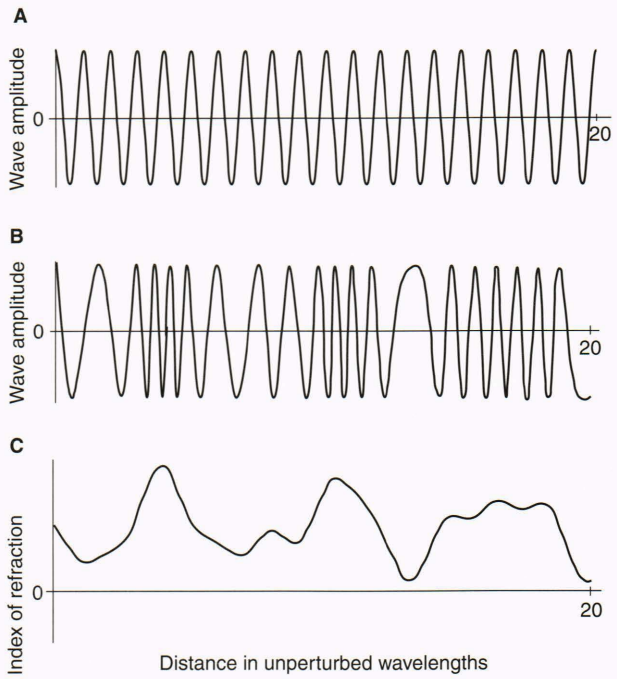

Figure 2. Illustration of phase shifts induced by a spatially variable index of refraction. **A.** Snapshot view of a monochromatic light wave as it travels over a distance of exactly 20 wavelengths. For this situation, the index of refraction is constant. Over this interval, the phase of the light has changed by 40π radians. **B.** A view of the same light wave shown in part A, but the wave is now traveling through a region where the index of refraction is varying about some mean value. (In the ocean, the mean value is taken to be 1.33). The distance of propagation is once again exactly 20 wavelengths. The actual phase change in the light wave is only 39.09π radians. This waveform was produced using Equation 1. **C.** The illustrative index of refraction field that was used in Equation 1 to produce the waveform shown in part B. Note how the wavelength increases for low values of the index and decreases for high values. The fractional index fluctuations shown are greatly exaggerated with respect to what would be encountered in the real ocean.

$$v = \frac{1}{2q}\dot{\phi}\,. \qquad (2)$$

This formula is also used to estimate mean fluid velocity within a scattering volume in LDV theory. Hence, the nonzero phase rates produced purely by index fluctuations are a source of contamination for LDV velocity measurements. When the phase rate is produced entirely by index fluctuations, we refer to the left side of Equation 2 as the equivalent velocity. The temporal spectrum of the equivalent velocity is of particular interest.

In this article we do not attempt to investigate the index of refraction field as a detailed function of space and time but rather use statistical techniques. We further assume that the Taylor approximation can be applied to the index field. That is, we ignore any intrinsic time dependence and assume that the dominant temporal effect comes from the rigid translation of spatial inhomogeneities at some velocity **U** through the optical path. In the context of Figure 1, this approximation may be expressed by writing $n(x,y,z,t) = n(x + Ut,y,z)$, where U is now the speed along

the x-axis. Since it is further assumed that the index of refraction field is a stationary random process, its three-dimensional wave-number spectrum $P_n(\mathbf{k})$ is defined by

$$P_n(\mathbf{k}) = \frac{1}{(2\pi)^3} \int d^3x\, e^{-i\mathbf{k}\cdot\mathbf{x}} \langle n(\mathbf{x}) n(0) \rangle , \tag{3}$$

where $\mathbf{k}$ is a given wave vector. Because statistics of the index fluctuations are assumed to have no preferred direction in space, $P_n(\mathbf{k}) = P_n(|\mathbf{k}|)$.

The basic idea is to use Equations 1 and 2 to relate the temporal spectrum of the observed phase rate to the index spectrum defined in Equation 3. After some algebra, one can write this spectrum as a two-dimensional integral over wave-vector components (k,m) as

$$\begin{aligned} P_v(\omega) &= \frac{1}{4q^2} P_{\dot{\phi}}(\omega) \\ &= \frac{\omega^2 L^2}{n_0^2 U} \int_{-\infty}^{\infty} dm \int_{-\infty}^{\infty} dk\, \mathrm{sinc}^2\left(\frac{Lk}{2}\right) \\ &\quad \times P_n\left(\sqrt{\frac{\omega^2}{U^2} + k^2 + m^2}\right) , \end{aligned} \tag{4}$$

where ω is the angular velocity in radians per second, P_v and $P_{\dot{\phi}}$ are, respectively, the equivalent velocity spectrum and the phase rate spectrum, and $\mathrm{sinc}(x) \equiv x^{-1}\sin x$. Equation 4 describes a combination of two effects operating in two perpendicular directions: a Doppler shift in the flow direction indicated by the appearance of the ω/U terms and a linear filtering along the optical path manifested by the sinc function. To proceed further it will be necessary to specify the index spectrum in more detail. In particular, we will make use of the Batchelor model,[4] which will in turn require a brief discussion of turbulence and microstructure theory.

Basic Turbulence and Microstructure Theory

The turbulent and scalar fields are assumed to be stationary random processes, and may be described by the universal Pao turbulent velocity spectrum and universal Batchelor scalar spectrum. The universal three-dimensional turbulent energy velocity spectrum,[5] assuming isotropy, is given by

$$E(k) = \alpha \epsilon^{2/3} k^{-5/3} \exp(-\eta k^{4/3}) , \tag{5}$$

where ϵ is the kinetic energy dissipation rate, k is the scalar wave number in radians per meter, $\eta = (3/2)\alpha k_K^{-4/3}$, and α is a universal constant. The kinetic energy dissipation rate is defined for an isotropic velocity field and a one-dimensional (longitudinal) measurement by $\epsilon = 15\nu\langle u_x^2 \rangle$, where u_x specifies the partial derivative of the x-component of fluid velocity with respect to x and ν is the kinematic viscosity of water (1×10^{-6} m^2/s). The Kolmogorov wave number $k_K = \epsilon^{1/4}\nu^{-3/4}$ defines the scale where the viscous forces equal the inertial forces. It was demonstrated in VBM that $E(k)$, also called the Pao universal velocity spectrum, displays excellent agreement with the Nasmyth empirical universal velocity spectrum[6] if α is 1.7. The Nasmyth spectrum is often used by ocean microstructure investigators.

In the stratified ocean, turbulence acts on the vertical gradients of temperature and salinity to produce microstructure or refractive fluctuations. The turbulent velocity field stirs or convects scalar variance to higher wave numbers. At scales smaller than the scale of the turbulent eddies, a strain field is induced that creates high-gradient scalar regions limited by molecular diffusion. Spectrally, this small-scale scalar field is described by the universal Batchelor spectrum. The universal three-dimensional Batchelor spectrum for a scalar γ, assuming isotropy, is given by*

$$G_\gamma(k) = C_\gamma k^{-1} e^{-\beta_\gamma k^2} , \tag{6}$$

where $C_\gamma = q_0 \chi_\gamma \nu^{1/2} \epsilon^{-1/2}$ and $\beta_\gamma = q_0 D_\gamma \nu^{1/2} \epsilon^{-1/2}$. The constant q_0 is bounded theoretically[7] by $\sqrt{3} < q_0 < 2\sqrt{3}$. Throughout this article, we have used the theoretical upper bound. The Batchelor wave number $k_B = \epsilon^{1/4}\nu^{-1/4}D_\gamma^{-1/2}$ defines the scale where the velocity associated with the molecular diffusion D_γ of the scalar γ equals the velocity of the small-scale strain field. The key turbulence statistics for the Batchelor spectrum are the kinetic energy dissipation rate and the dissipation rate of the scalar variance χ_γ. The Batchelor spectrum has two subranges: a viscous-convective subrange (k^{-1}) in which the scalar field is controlled by the strain field and the effects of molecular diffusion are unimportant, and the viscous-diffusive subrange (exponential roll-off) in which the molecular diffusion counterbalances the convection of larger-scale features to smaller scales by the strain field. If an inertial subrange exists in the velocity field, an inertial-convective subrange ($k^{-5/3}$) would exist in the scalar spectrum at wave numbers smaller than the transition wave number $k_* = C_* k_K$ ($C_* = 0.03$ to 0.04; Ref. 8). The strain field, whose root-mean-square magnitude is on the order of $(\epsilon/\nu)^{1/2}$, is not as efficient as the turbulent eddies for convecting scalar variance to higher wave numbers. This inefficiency is manifested in the shallower spectral slope in the scalar spectrum for the subrange dominated by the strain field, compared with the inertial-convective subrange. An inertial subrange is not required to obtain a Batchelor spectrum. The low-wave-number end of the viscous-convective subrange of the Batchelor spectrum, however, is expected to begin at about the same transition wave number that would be anticipated if an inertial-convective subrange were present.

The Batchelor temperature and salinity spectra depend on the kinetic energy dissipation rate and the dissipation rates of temperature and salinity variance, which are defined, respectively, assuming isotropy and for one-dimensional (longitudinal) measurements, by $\chi_T = 6D_T\langle T_x^2 \rangle$ and $\chi_S = 6D_S\langle S_x^2 \rangle$. The molecular diffusion rates of tem-

*Following the conventions used in the microstructure literature, the spectra in Equations 5 and 6 are normalized so that the amount of variance lying in a spherical shell of thickness dk in wave-number space is simply given by the product of dk and the corresponding spectrum. For a spectrum normalized as in Equation 3, an extra factor of $4\pi k^2$ is required.

perature (heat) and salinity, D_T and D_S (1.4×10^{-7} and 1.4×10^{-9} m^2/s), respectively, control, in conjunction with the kinetic energy dissipation rate, the location of the roll-off region of the temperature and salinity spectra. Because of the smaller—by a factor of 100—molecular diffusion rate of salt compared with temperature, the Batchelor salinity spectrum extends a decade higher in wave-number space than the temperature spectrum.

In the stratified ocean, the three-dimensional refractive index spectrum can be expressed in terms of its temperature and salinity counterparts by the relation

$$4\pi k^2 P_n(k) = n_T^2 G_T(k) + n_S^2 G_S(k) + 2 n_T n_S \, \mathrm{Re}[G_{TS}(k)], \quad (7)$$

where n_T and n_S (-1.1×10^{-4} °C^{-1} and 1.9×10^{-4} [ppt]$^{-1}$ at 20°C) are the partial derivatives of the refractive index with respect to temperature and salinity, respectively. The quantity $\mathrm{Re}[G_{TS}(k)]$ is the real part of the cross-spectral density of temperature and salinity.

Since the Batchelor spectrum is used to model the refractive index spectrum, the key turbulence parameters for predicting the equivalent velocity spectrum induced in LDV measurements by the refractive index field are the kinetic energy dissipation rate ϵ and the dissipation rates of temperature and salinity variances χ_T and χ_S, respectively. The other flow-field-related parameter important for the model predictions is the mean speed U.

Spectral Prediction

The equivalent velocity spectrum shown in Equation 4 becomes

$$P_V(\omega) = \frac{4|\omega| L^2 n_T^2}{n_0^2} C_T J\left(\frac{\omega L}{2U}, \frac{\beta_T \omega^2}{U^2}\right) + \frac{4|\omega| L^2 n_S^2}{n_0^2} C_S J\left(\frac{\omega L}{2U}, \frac{\beta_S \omega^2}{U^2}\right), \quad (8)$$

where the cross-term in Equation 7 has been assumed to vanish. The function $J(a, b)$, unfortunately, cannot be evaluated in closed form. It is given by

$$J(a,b) \equiv \frac{b}{2} \int_0^{\pi/2} d\alpha \, \sec^2\alpha \, \mathrm{sinc}^2(a \tan\alpha) \times \exp\left(-\frac{b}{2}\sec^2\alpha\right) \times \left[K_1\left(\frac{b}{2}\sec^2\alpha\right) - K_0\left(\frac{b}{2}\sec^2\alpha\right)\right]. \quad (9)$$

Here K_0 and K_1 are modified Bessel functions as conventionally defined.[9] Equation 8, which will be compared later with empirical findings, is the main theoretical result of this work.

A plot of $P_u(f)$, where f is frequency in Hertz, is shown for a towed system and typical oceanic parameters in Figure 3. Also shown for comparison is the turbulence spectrum calculated on the basis of Equation 5 that would be measured by a "perfect" LDV system. As previously discussed, the molecular diffusion constant of salinity is two orders of magnitude smaller than that of temperature. Hence, salinity microstructure persists up to substantially higher wave numbers, with the result that P_u has a double roll-off. The relative impact of the temperature and salinity fields within the overlapping region of the refractive spectrum will depend on the relative magnitudes of the vertical temperature and salinity gradients. In the ocean, the refractive spectrum will always be dominated by the salinity field for wave numbers or frequencies beyond the Batchelor temperature wave number.

Optical Heterodyning

We will describe here the approach used to convert the measured photocurrent to an equivalent velocity spectrum. Readers familiar with demodulation concepts may wish to skip to the next section.

Considerable care and some indirectness of approach are clearly necessary to measure the phase of an electromagnetic field having a wavelength on the order of only a few thousand atomic diameters and a frequency on the order of a thousand trillion cycles per second—far more rapid than anything to which an electronic circuit can directly respond.

Optical phase can be measured by the conversion of superimposed light waves into a photocurrent, which is subsequently analyzed. If Figure 1 were drawn in more detail, it would show that a reference beam is split off

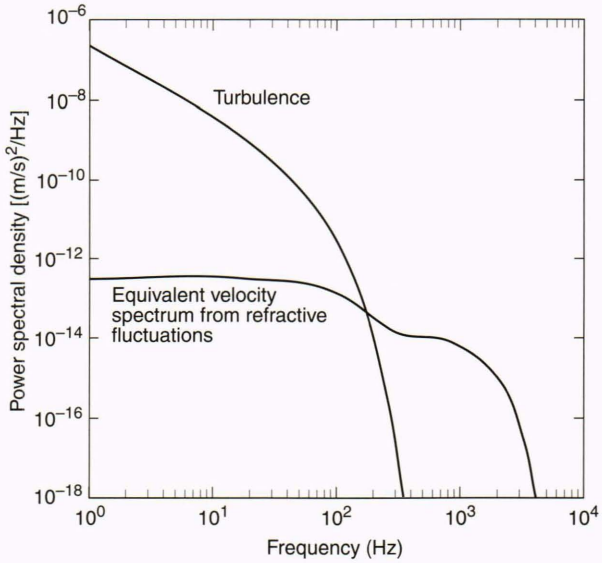

Figure 3. Equivalent velocity spectrum prediction based on Equation 8 compared with turbulent velocity spectrum as measured by an "ideal" laser-Doppler velocimeter (LDV). The turbulent velocity spectrum is based on Equation 5. This plot illustrates weak oceanic turbulence. The kinetic energy dissipation rate $\epsilon = 2.0 \times 10^{-10}$ m^2/s^3, the dissipation rate of temperature variance $\chi_T = 3.0 \times 10^{-10}$(°C)^2/s, and the dissipation rate of salinity variance $\chi_S = 5.0 \times 10^{-12}$(ppt)^2/s. In addition, we have assumed speed $U = 5$ m/s and the distance to the scattering volume $L = 10$ m.

from the source, shifted in frequency an amount ω_b by Bragg cells, and projected onto the photosensitive surface of the receiver, where it is combined with the beam reflected from the mirror. It is this optical heterodyning process that produces the observed photocurrent $J(t)$.

To understand the photocurrent, it is necessary to model the electromagnetic field to some extent. We can make several simplifying assumptions from the outset. First, since the light source is taken to be monochromatic and the radiation field is treated as a scalar, polarization effects are ignored. Second, since all speeds associated with mechanical vibrations and microstructure advection are completely negligible compared with the speed of light, we assume at the beginning that all of these velocities can initially be ignored and derive a static expression for the photocurrent, whose only time dependence is associated with that of light propagating through a frozen medium. The medium and the environment are then unfrozen, and the new photocurrent is simply taken to be the static expression, with the index of refraction and other relevant variables allowed to depend explicitly on time.

We first establish notation for the electric field. Let $E(\mathbf{x},t)$ denote the electric field at some arbitrary point in space and time. For monochromatic radiation of angular frequency ω_0 and static boundary conditions we may write

$$E(\mathbf{x},t) = A(\mathbf{x})\cos[\omega_0 t + \phi(\mathbf{x})], \tag{10}$$

where $A(\mathbf{x})$ and $\phi(\mathbf{x})$ are, respectively, the amplitude and phase, which are both functions of the position $\mathbf{x}$. All of the quantities in Equation 10 are real. Using an asterisk to denote the complex conjugate, it can be written in the form

$$E(\mathbf{x},t) = \frac{1}{2}E(\mathbf{x})e^{-i\omega_0 t} + \frac{1}{2}E^*(\mathbf{x})e^{i\omega_0 t}, \tag{11}$$

where $E(\mathbf{x})$ is a complex electric field amplitude given by $E(\mathbf{x}) = A(\mathbf{x})e^{-i\phi(\mathbf{x})}$. To save space, equations like 11 will often be written in the form

$$E(\mathbf{x},t) = \frac{1}{2}E(\mathbf{x})e^{-i\omega_0 t} + \text{c.c.}, \tag{12}$$

where c.c denotes complex conjugate.

The Photocurrent as a Surface Integral

The photocurrent produced at the detector is given by the surface integral

$$J(t) = 2M\int_S E^2(\mathbf{x},t)d^2x, \tag{13}$$

where S denotes the photosensitive surface of the detector and M is a proportionality constant that depends on the details of the detection device. Near the detector we may write

$$E(\mathbf{x},t) = \frac{1}{2}E_m(\mathbf{x})e^{-i\omega_0 t} + \frac{1}{2}E_r(\mathbf{x})e^{-i(\omega_0+\omega_b)t} + \text{c.c.}, \tag{14}$$

where E_m and E_r, respectively, denote the mirror-reflected and the reference-beam electric field amplitudes. Unless specified otherwise, the position vector $\mathbf{x}$ will from now on be restricted to lie on S. When we square $E(\mathbf{x},t)$, all quantities that oscillate near the optical frequency are automatically filtered out by the electronics and, for purposes of calculating the photocurrent, we may write

$$E^2(\mathbf{x},t) = \frac{1}{2}|E_m(\mathbf{x})|^2 + \frac{1}{2}|E_r(\mathbf{x})|^2 + \frac{1}{2}[E_m(\mathbf{x})E_r^*(\mathbf{x})e^{i\omega_b t} + \text{c.c.}]. \tag{15}$$

The first two contributions to E^2, called the pedestal, do not need to be analyzed in detail for present purposes. If ω_b is high enough, these contributions will fluctuate at a comparatively much lower frequency when the component vibrations and index fluctuations are unfrozen; hence, they can be eliminated with a high-pass filter. We may therefore write

$$J(t) = Me^{-i\omega_b t}\int_S E_m^*(\mathbf{x})E_r(\mathbf{x})d^2x + \text{c.c.} \quad . \tag{16}$$

Demodulation—The Complex Photocurrent

Equation 16 is the static expression mentioned previously. The expression for the situation where the medium and environment are allowed to fluctuate is thus taken to be

$$J(t) = Me^{-i\omega_b t}\int_S E_m^*(\mathbf{x},t)E_r(\mathbf{x},t)d^2x + \text{c.c.}, \tag{17}$$

where the reference and mirror-reflected electric field amplitudes are now allowed to depend explicitly on time. The photocurrent now contains a range of frequencies. It is assumed, however, that ω_b is large enough that $J(t)$ is still a narrowband process.

The complex photocurrent $C(t)$ as the output of a filter acting on the real photocurrent $J(t)$ is defined according to

$$C(t) \equiv \int d\tau\, w(\tau)e^{i\omega_b(t+\tau)}J(t+\tau), \tag{18}$$

where $w(\tau)$ is a filter weighting function, whose exact form is not crucial so long as it meets certain general criteria. For our work, we chose a Gaussian specified by

$$w(\tau) = \frac{1}{\sqrt{2\pi}\tau_0}\exp\left(-\frac{\tau^2}{2\tau_0^2}\right). \tag{19}$$

Let $\Delta\omega$ be the spectral width of $J(t)$. For a narrowband process we have $\Delta\omega << \omega_b$. The most important requirement for the filter weighting function is that it vary over an appropriate time scale, which will hold if $\omega_b^{-1} << \tau_0 << \Delta\omega^{-1}$. With this condition in place, we can say that the parts of $J(t)$ not involving ω_b vary so slowly that they can be taken outside of the integral in Equation 18. Remembering to include the complex conjugate portion, this means that

$$C(t) = M\int_S E_m^*(\mathbf{x},t)E_r(\mathbf{x},t)d^2x\int w(\tau)d\tau + Me^{2i\omega_b t}\int_S E_m(\mathbf{x},t)E_r^*(\mathbf{x},t)d^2x \times\int w(\tau)e^{2i\omega_b\tau}d\tau \ . \quad (20)$$

The first integral over τ in this relation is unity. The second integral, on the other hand, is extremely small by virtue of the property $\omega_b\tau_0 >> 1$ and hence can be ignored; therefore,

$$C(t) = M\int_S E_m^*(\mathbf{x},t)E_r(\mathbf{x},t)d^2x \ . \quad (21)$$

The measurement and analysis of the complex photocurrent are the central themes of this work. Let the in-phase and quadrature components of C be denoted by I and Q, respectively, so that

$$C(t) = I(t) + iQ(t) \ . \quad (22)$$

Note that C traces out a trajectory in the complex plane as time advances. The nature of this trajectory is determined by the fluctuations encountered by the mirror-reflected and reference beams as they make their separate ways to the face of the detector. Several experimental trajectories are discussed later in this article.

Vibrations

An ideal reference beam from a "perfect" laser will be aligned so that it has some constant phase ψ_r over the photosensitive surface, or $E_r(\mathbf{x},t) = e^{i\psi_r}$. If there are no index fluctuations and no component vibrations to perturb the mirror-reflected beam, we may likewise write $E_m(\mathbf{x},t) = e^{i\psi_m}$; hence,

$$C(t) = MAe^{i(\psi_r - \psi_m)} = C_0 \ , \quad (23)$$

where A is the effective area of the detector. That is, $C(t)$ should be "stuck" at some fixed point in the complex plane. It is precisely this condition that one attempts to achieve in preliminary experiments designed to minimize the system noise.

Suppose now that this ideal situation is disturbed only by an oscillating mirror, so that the distance L is actually $L + \eta(t)$. Then $E_m(\mathbf{x},t) = e^{i[\psi_m + 2q\eta(t)]}$ or

$$C(t) = C_0e^{-2iq\eta(t)} \ , \quad (24)$$

where q is the wave vector in air or water, depending on where the mirror is located. Now we should observe $C(t)$ swinging back and forth through C_0 in a circular arc centered on the origin. Every time the mirror moves through half an optical wavelength, $C(t)$ will trace out a complete circle in the complex plane. When several sources of vibration are present, $C(t)$ will exhibit the same type of behavior. By performing a careful sequence of preliminary experiments that measure $C(t)$ under a variety of conditions, it is possible to understand and quantify vibration noise in considerable detail.

Refractive Index Fluctuations

Now consider the opposite situation. That is, suppose there are no mirror or component vibrations but that index of refraction fluctuations are present. Then we write $E_m(\mathbf{x},t) = e^{i[\psi_m + i\phi(t)]}$, where $\phi(t)$ is given by Equation 1. We then have

$$C(t) = C_0e^{-i\phi(t)} \ . \quad (25)$$

Equations 24 and 25 reemphasize the well-known result that index of refraction fluctuations can masquerade as mirror vibrations or equivalently as scattering particle motion in a backscatter reference-beam LDV. Note that Equation 25 needs to be modified if the optical fluctuations are strong enough for there to be amplitude as well as phase effects.

For a measured $C(t)$, the equivalent velocity is defined by

$$v = \left(\frac{1}{2q}\right)\frac{d}{dt}\tan^{-1}\left(\frac{Q}{I}\right) = \left(\frac{1}{2q}\right)\frac{I\dot{Q} - Q\dot{I}}{I^2 + Q^2} \quad (26)$$

or $v = -\dot{\eta}(t) =$ mirror velocity if Equation 24 applies. Likewise, $v = -\dot{\phi}/2q$ when Equation 25 applies. The challenge for the experimental design is to have $\dot{\phi}$ dominate over vibration and other phase effects so that Equation 8 can indeed be verified.

EXPERIMENTAL DESCRIPTION

Motivation and Philosophy

To validate our predictions for the optical phase fluctuations (Equation 8), laboratory experiments were planned and executed over a range of parameters that included relevant oceanographic values. The critical parameters are path length L, mean speed U, turbulence dissipation ϵ, temperature dissipation χ_T, and salinity dissipation χ_S. To reduce the complexity somewhat, we decided to perform the first sequence of experiments without salinity variations. The index of refraction fluctuations for these experiments were produced by temperature variations only. Hence, the second term in Equation 8 is zero.

The experiments were performed in an open-channel recirculation flow channel in the APL Hydrodynamics Laboratory shown schematically in Figure 4. A sensitive laser system (interferometer/LDV) was mounted on two optical tables joined across the 0.88-m-wide flow channel. Turbulence was produced by flow past a grid upstream of the optical path, and temperature fluctuations were created by injecting heated water through holes in the grid. Since the turbulence levels are related to the flow past the grid, low speeds (5, 10, and 15 cm/s) were used so that the resultant turbulence dissipations would in-

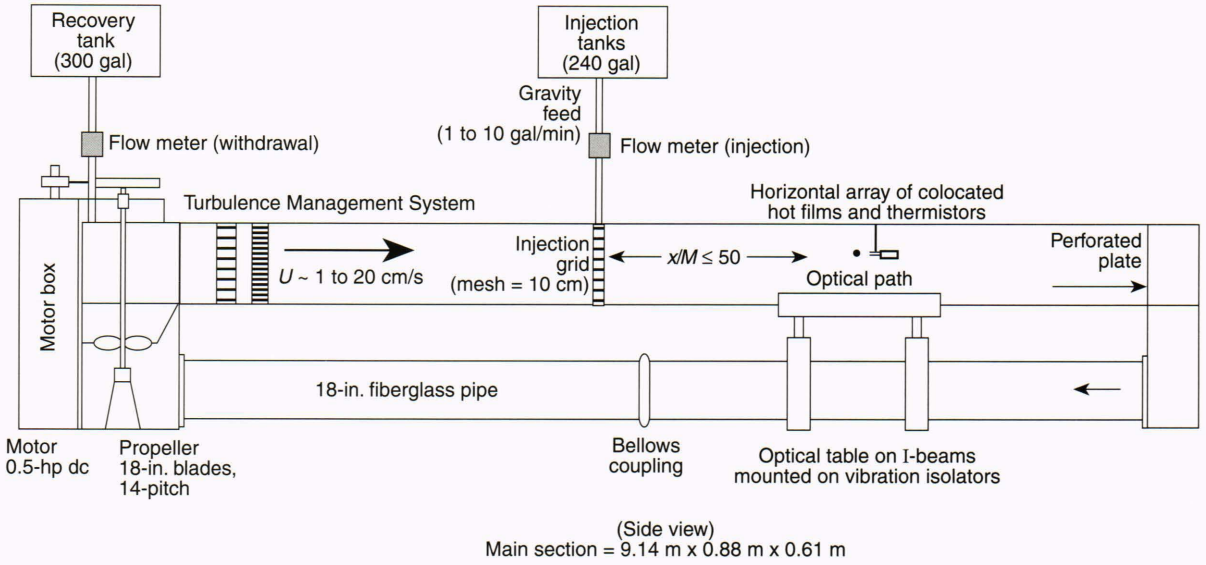

Figure 4. Flow channel and injection system schematic (U = speed, x/M = distance from injection grid to optical path divided by grid mesh size).

clude levels observed in the ocean. Velocity was measured with three hot-film anemometers spaced across the tank at the depth of, and just downstream of, the laser beam, and temperature was measured with three thermistor sensors located near the hot-film probes. To achieve low-noise optical measurements, the optical system was mounted on vibration-isolation legs, the flow channel was mounted on vibration-isolation pads, optical windows were reinforced with struts, and some experiments were performed in the early morning hours when most building machinery was turned off. Some of the relevant experimental details follow in the next three sections.

Flow Channel and Injection System

Ideally, the velocity and temperature fields across the test section will be isotropic, statistically homogeneous, and stationary. The objectives for the injection system are to provide a uniform injection of water at a desired temperature while maintaining a constant mean flow through the recirculating flow channel. To obtain accurate measurements of ϵ and χ_T, accurate calibrations of the hot-film and thermistor sensors and measurement of signals over a large dynamic range are required.

The 0.5-hp dc motor has feedback control to maintain the motor rpm and mean channel flow rate to within $\pm 1\%$. The nominal range of available mean flow speeds is 1 to 20 cm/s. Low ambient turbulence levels are necessary to ensure that the velocity field downstream of the grid is dominated by the grid and that flow conditions are reproducible. A turbulence management system consisting of perforated plates, honeycombs, and screens is used to reduce the incoming turbulence levels to 0.75% ($100\ \langle u^2 \rangle^{1/2} / U$, where U is the mean flow speed and u is the turbulent component). The flow exits the test section through a perforated plate. The perforated plate accelerates the exit flow speed to above the surface wave speed and eliminates reflection of surface waves back into the test section.

The temperature control system comprises two heaters (10 kW each), a thermostat, and an Apple computer, and is used to control the heaters to achieve and maintain the desired overheat. The water is circulated through the two supply tanks (120 gal each) by a pump to ensure an even temperature distribution throughout the two tanks.

No effort is made to maintain a constant mean temperature in the channel during the course of a run. The water in the injection system supply tanks was typically heated to 25°C over the ambient temperature of the water in the flow channel. The mean temperature of the flow channel is monitored by a platinum resistance thermometer during a run. Increases by about 1°C at the maximum injection rate of 10 gal/min are observed over the duration of a test run. Such increases reduce the temperature contrast at the grid injection points by a maximum of 4%. A withdrawal system made up of a digital flowmeter, a pump, and a reserve tank is used to maintain a constant mean flow in the channel by withdrawing fluid at the same rate that the injection system puts fluid into the channel.

The combination of gravity feed and a digital flowmeter ensures a constant injection rate through the hollow injection grid. The square mesh injection grid is constructed from hollow Plexiglas cylinders having a diameter d of 1.905 cm with a total of 550 injection points (0.32-cm dia.). Constant injection rates for the experiments ranged from 1 to 10 gal/min. The center points of the rods are separated by 10 cm, yielding a mesh size M of 10 cm and a ratio M/d of 5.25. Mean speeds for the test runs ranged from 5 to 15 cm/s, yielding a range of grid Reynolds numbers ($\mathrm{Re}_M = UM/\nu$) of 5000 to 15,000, respectively. The wide range of velocity and scalar length scales generated by the grid is shown in Figure 5.

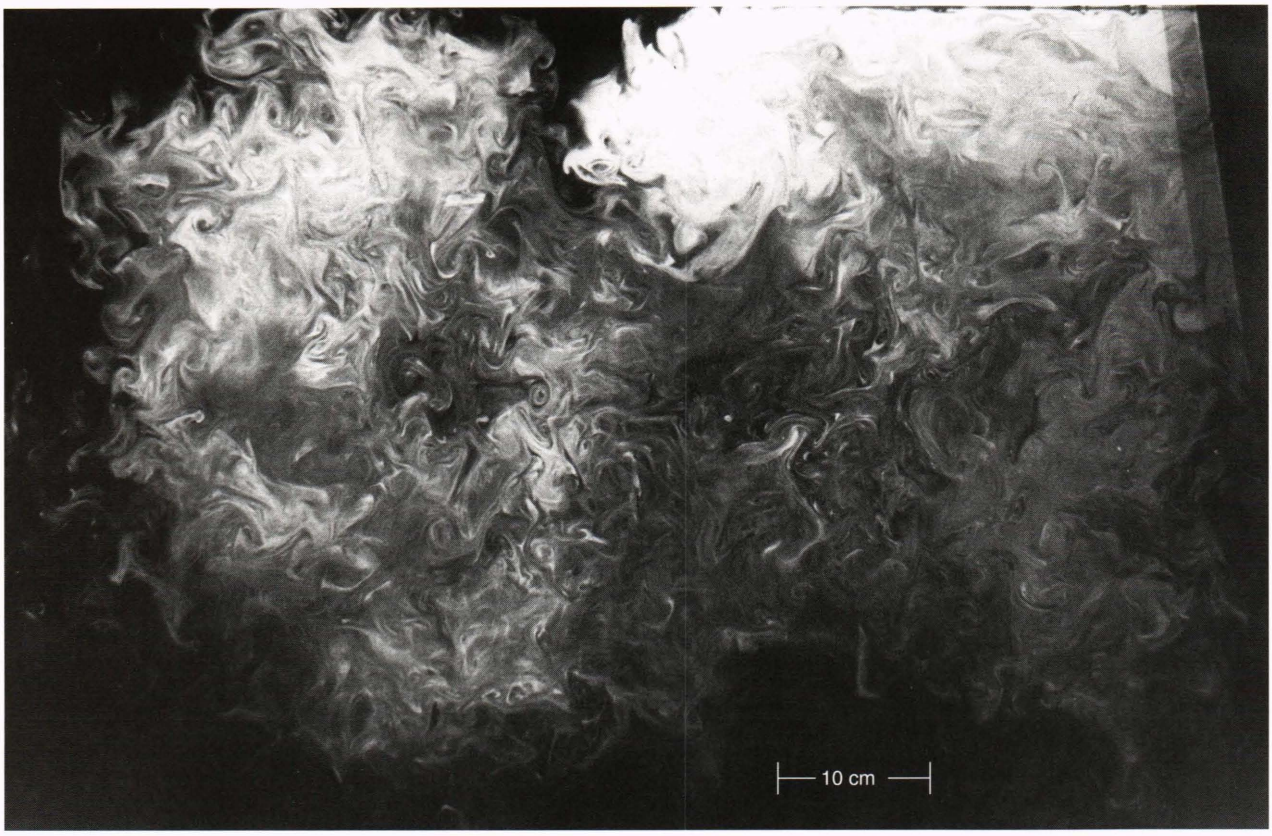

Figure 5. Photograph of dye pumped through the injection system at 10 gal/min and illuminated by a thin sheet of laser light showing the wide range of scales associated with turbulence-induced microstructure.

Ground Truth Measurements

An array consisting of three pairs of colocated hot-film velocity sensors and thermistors is used to quantify the velocity and temperature field. The hot-film and thermistor sensors in each pair are separated by 1 cm. Two of the sensor pairs are located 10 cm away from the sidewalls of the flow channel. The estimates of ϵ and χ_T from the third pair, located at the center of the flow channel, are used as the inputs to the spectral predictions for $P_u(\omega)$ implied by Equation 8. Cross-tank dye line measurements indicate that the mean speed is uniform over about 70% of the flow channel. The outer sensor pairs are used to bound the variability in the turbulence statistics during an injection run.

Let G_u and G_T be spectral estimates of the turbulent velocity and temperature fluctuations, respectively. Then the estimates of ϵ and χ_T are determined according to

$$\epsilon = 15\nu \int_{k_0}^{k_1} k^2 G_u(k)\,dk \qquad (27)$$

and

$$\chi_T = 6D_T \int_{k_0}^{k_1} k^2 G_T(k)\,dk\,. \qquad (28)$$

The high-wave-number portions of the velocity and temperature gradient spectra dominate both estimates. To resolve the velocity and temperature gradient variance, the high-wave-number cutoffs should be on the order of the Kolmogorov and Batchelor wave numbers, respectively. The measurements obtained during the experiments generally satisfied this criterion. Variance-preserving plots of the velocity and temperature gradient spectra are examined in conjunction with the measured noise characteristics to determine the high-wave-number cutoffs for the integrations described in Equations 27 and 28. The integrations are cut off just before the wave number where noise dominates the spectra. The variance-preserving plots also indicate whether the variance was resolved. These statistics are relatively insensitive to the selection of the low-wave-number cutoff. In most experimental results, k_0 corresponds to about 1 cycle per meter (cpm).

The hot-film sensors are conical Thermo-Systems Incorporated probes with a 0.27-mm-dia. ring of platinum, and are fairly rugged. The spatial response of the sensors is sufficient to resolve the velocity field generated during these experiments down to at least the Kolmogorov scale. The measured velocity spectrum is occasionally cut off slightly before the Kolmogorov scale, owing to noise.

The hot-film sensors are dynamically calibrated *in situ* over a small velocity range about the mean speed by oscillating the sensors before and after the sequence of injection runs. Calibration errors of less than 1% were reported by Perry and Morrison[10] using a similar approach.

The thermistors were calibrated over a temperature range of 18 to 28°C. Over this range, the thermistor calibration curve is linear. Although the injection temperature at the grid is nominally 47°C, mixing with the ambient water (typically 22°C), coupled with the small injection volume rate relative to the ambient volume rate passing by the grid, reduces the overall temperature fluctuation range to around 50×10^{-3} °C at the test section.

Correction of the measured temperature spectrum is required to obtain accurate estimates of χ_T, since the frequency response of the thermistors is not sufficient to resolve the underlying temperature spectrum. Two approaches to determining the speed-dependent thermistor transfer functions are used. The first approach to estimating the thermistor transfer function involves operating the thermistor as a velocity sensor and making direct comparisons with the colocated hot-film measurements under the conditions of grid turbulence without injection. In the second method, it is assumed that the underlying temperature spectrum is described by the Batchelor spectrum.

The first approach has the advantage of directness. The hot-film sensors are limited only by their spatial response and are not frequency-response limited. The frequency response of the thermistor is obtained from the ratio of the thermistor and hot-film velocity spectrum in frequency space. This approach requires a relatively strong turbulent velocity field that extends to frequencies relevant to the temperature field created during a grid injection run. The grid was located at x/M of 10 to create a strong turbulent velocity field, and corrections for thermistor response were obtained for mean speeds of 10 and 15 cm/s. The closest x/M used for the injection experiments was 15. Attempts to utilize this approach for a mean speed of 5 cm/s were unsuccessful because of the relatively weak and limited frequency range of the turbulent velocity field. The Batchelor approach is used to estimate the thermistor frequency response for the 5 cm/s runs on the basis of the injection runs at x/M of 15.

Optical System

The optical system needed to be analogous to a backscatter LDV reference beam system but free of effects from true particle velocity within an LDV probe volume. To achieve those conditions, we used a backscatter system where such probe volume effects have been removed by replacing the probe volume with a mirror. The resulting system can be viewed either as a reference-beam backscatter LDV or as an interferometer. It will be instructive to consider those two alternative interpretations separately.

First, let us consider the system as a backscatter LDV. Figure 6 is a schematic of the optical configuration, and Figure 7 is a photograph of the actual system. The laser is a 50-mW Spectra-Physics Model 125 He–Ne unit with a wavelength in air of 632.8 nm. The laser beam is directed via two mirrors through a variable attenuator to a beam splitter, where part of the beam is expanded and collimated to about a 1-cm diameter and then passes through the 6-in. optical window across the tank (L = 0.88 m) to a mirror on the other table. The beam returns

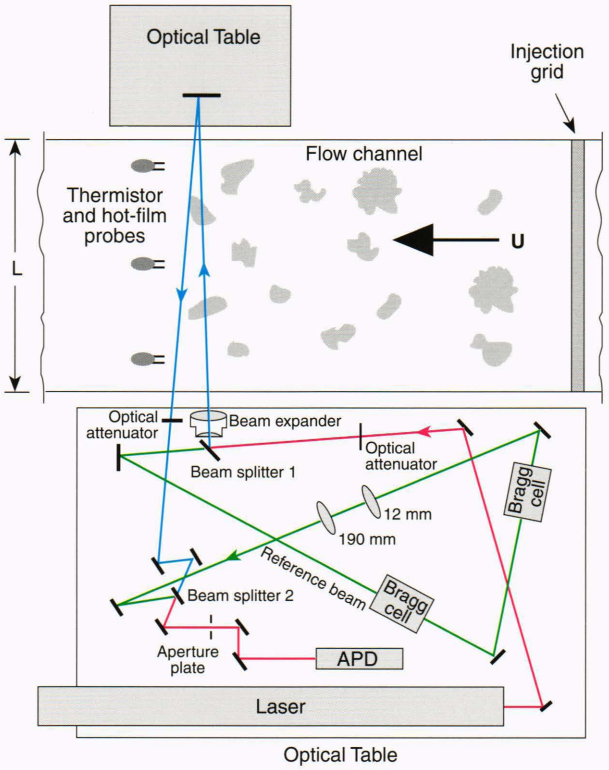

Figure 6. Schematic of backscatter optical system used to investigate effects of refractive fluctuations. The blobs represent the fluctuations as they are moved along with speed U. The photocurrent is formed at the face of the avalanche photodiode (APD).

through the flow channel and an optical attenuator and is recombined with the reference beam at the second beam splitter.

The reference beam formed at the first beam splitter passes through two Bragg cells (acousto-optic cells that produce a frequency shift via diffraction by acoustic waves). They are driven to provide two outputs, one a fixed 40-MHz signal and the other an adjustable frequency (in 1-Hz increments) between 38 and 42 MHz. The Bragg cells are oriented so that the upshifted diffraction order from the first cell passes through the second. The downshifted order from the second Bragg cell is then used. The resultant light is shifted by the difference frequency between the two Bragg cells. No shift is obtained if both cells are set at 40 MHz (the condition used in aligning the system). The beam from the final Bragg cell is expanded to the diameter of the transmitted beam by the next two lenses and recombined with the transmitted light at the next beam splitter. The path length of the reference beam has been matched to the optical path of the transmitted beam to within the coherence length of the laser. The recombined beam is directed through a 0.5-mm hole on an aperture plate. The 0.5-mm beam is then directed to the photodetector housing, which incorporates a 632-nm line filter and a 90-mm lens to focus the collected light onto the detector, a temperature-compensated avalanche photodiode (APD) with a 0.76-mm-dia. sensing area.

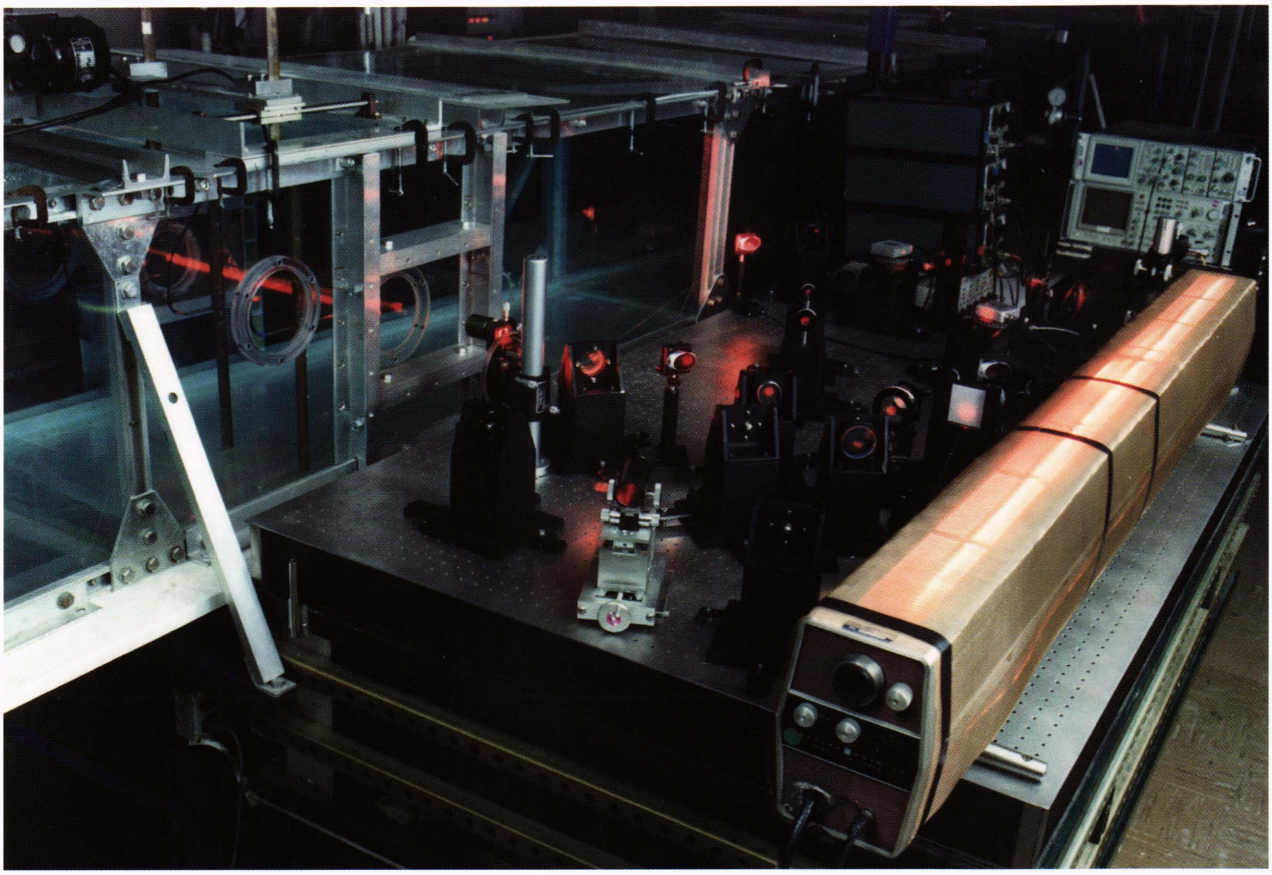

Figure 7. Photograph of the optical system used in refractive experiments and shown schematically in Figure 6.

The reference beam has been shifted in frequency 7 kHz by the two Bragg cells at 40 MHz and 40,007,000 Hz. For zero mirror motion and in the absence of phase variations caused by refractive fluctuations along the optical path, the photocurrent will be monochromatic at 7 kHz (the beat frequency between the direct and reference beams). Variations due to refractive fluctuations being swept past the optical beam will cause a broadening of the photocurrent spectral peak at 7 kHz, as will vibrations of the mirror. The photocurrent is recorded on a Masscomp data acquisition/computer system, and is demodulated in software using Equations 18 and 22 to obtain the in-phase and quadrature components of the complex photocurrent. Optical phase follows immediately, and equivalent velocity is determined on the basis of Equation 26. The equivalent velocity spectrum can then be calculated.

The optical system can also be considered as an interferometer with one arm passing through the flow channel and the other passing through air on the optical table. If the Bragg cells are set so that both are driven at 40 MHz, the resultant frequency shift is zero. In this case the two arms of the interferometer have the same frequency and, when the two beams are recombined at the beam splitter, an interference pattern results caused by any small misalignment of the two wave fronts from each arm. The interference pattern is changed by fine adjustments of the optics until the detector aperture is smaller than the fringe spacing (0.5 and 2 mm, respectively). Any motion of the mirror or optical path-length changes resulting from index of refraction variations in the flow channel will affect the fringe pattern. For an optical path-length change equivalent to one wavelength (such as caused by a mirror displacement of one-half wavelength), a detector whose size is small compared with the fringe pattern will alternately encounter a maximum and a minimum in the fringe pattern. The time rate of change of the photodetector output resulting from the path length changes can be interpreted in terms of the mirror motion or refractive variations in the water.

The alignment of the system is performed with the Bragg cells set for zero net frequency shift, and the optics are adjusted until a fringe pattern is achieved at the aperture plate. With the Bragg cells driven for no net frequency shift of the reference arm, the system is equivalent to an interferometer. Once the system is aligned, the Bragg cells are set for a net frequency shift of 7 kHz to move the photocurrent center frequency away from baseband—a condition necessary for proper demodulation. This shift causes the fringes to be swept across the detectors, giving rise to the photodetector signal at 7 kHz. With the reference beam so shifted, the system is analogous to a reference beam LDV without a probe volume. These two viewpoints have proved quite useful for interpreting the results and comparing them with the predictions for the equivalent velocity spectrum previously discussed.

RESULTS AND CONCLUSIONS

Equivalent Velocity Spectra

We discuss here the results of several experimental runs that illustrate most of the pertinent aspects of the observations. Because the theoretical predictions depend on the turbulence strength (through ϵ), the scalar microstructure strength (through χ_T), as well as the path length and mean speed, we planned the experimental sequences so that most of the parameters would be kept constant to determine the dependence on the remaining variable. In particular, we determined the dependence on χ_T by keeping the mean speed constant, the grid at a fixed location (constant turbulence), and the path length constant. Five experimental runs were conducted at 9.8 cm/s with the grid 150 cm upstream of the laser path ($x/M = 15$). The runs consisted of (a) ambient (no injection), (b) 1 gpm (gallon per minute) injection, (c) 3 gpm, (d) 6 gpm, and (e) 10 gpm.

Figure 8 shows the measured temperature and velocity spectra for each of the four injection runs (b through e). The velocity spectra are consistent and display excellent agreement with the Pao universal velocity spectrum (on the basis of the average ϵ from these four runs) for scales smaller than the grid mesh size $M = 10$ cm (k greater than 10 cpm). For our experiments, the turbulent velocity field created by the grid for scales smaller than 10 cm should be approximately isotropic[11] for downstream distances x/M greater than 10 to 15, and display good agreement with the universal spectrum for wave numbers greater than 10 cpm. To generate an inertial subrange in the velocity field, the Reynolds number of the grid should be greater than 10^6. The low Reynolds numbers of these experiments (5000 to 15,000) imply that an inertial subrange ($k^{-5/3}$) should not be observed in the velocity spectra; nor should an inertial–convective subrange ($k^{-5/3}$) be observed in the temperature spectra. The Batchelor spectra for each run are shown for comparison with the measured temperature spectra. The agreement is best in the roll-off region, with differences less than a factor of 2 observed at wave numbers greater than 2 cpm. The Batchelor spectrum is expected to begin at about 7 cpm. A break in the spectral slope (droop below k^{-1}) for the three highest injection runs occurs between 2 to 5 cpm. Similar behavior is observed for velocity spectra.

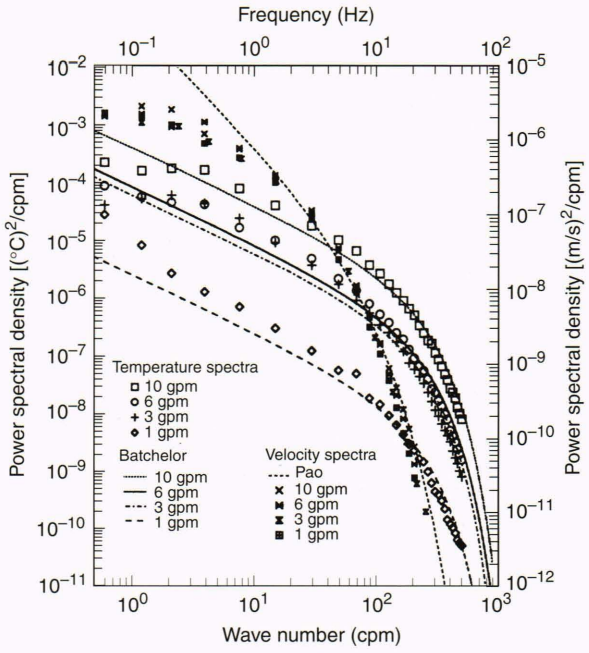

Figure 8. Comparison of the universal Pao and Batchelor spectra (Eq. 5 and 6) with measured results. These results correspond to the results shown in Figure 9 (gpm = gallons per minute, cpm = cycles per meter).

We have determined the effect of the resulting refractive fluctuations on the optical path by calculating the complex photocurrent from the observed real photocurrent as described by Equations 18 and 22. Figure 9 shows the resulting in-phase (I) and quadrature (Q) components in the phasor plots for the first 0.5 s of data. Note that the phasor trajectory for the no-injection case is nearly a circle rather than being fixed at a constant angle. The circular phasor trajectory is due to small residual window and mirror vibrations. As the temperature injection increases, we see that the phasor trajectory becomes more complicated. For weak injections, the phasor generally sweeps out various arcs with a nearly constant radius. For the strongest injections, the phasor not only sweeps out arcs, but its magnitude also varies and sometimes nearly passes through the origin. These amplitude variations, as also evidenced in the photocurrent time series, may be due to interference from rays within the finite beam width caused by path length variations. Because the strongest refractive conditions that produce this effect start to violate some of the simplifying assumptions of the basic prediction given by Equation 8, these phasor amplitude variations are not predicted by the model.

The phase, phase rate, and equivalent velocity were computed for each of these experiments. The equivalent velocity spectra are shown in Figure 10, along with the VBM model prediction for the appropriate values of ϵ and χ_T. The spectra were computed over 54 s of data after low-pass filtering at 5 kHz and subsampling at 25,000 samples/s. The bottom dashed curve in both Figures 10A and 10B represents the system noise level for the "no injection" condition. The spectral peaks near 10 and 30 Hz are associated with window vibrations, and the peaks near 100 Hz are due to component vibrations. The system noise level is below 10^{-14} $(m/s)^2/Hz$ out to about 6 Hz, or about 3 orders of magnitude below the spectral level for the strongest refractive signal shown in Figure 10B. Hence, over much of the frequency regime of refractive signals, the system noise levels are small enough to allow direct comparison of experimental results with spectral predictions over a reasonable frequency range.

In general, reasonable agreement exists between the experimentally determined spectra and the VBM prediction. For the two injection runs shown in Figure 10A (1 March 1991/Run Nos. 7 and 8), the spectral levels are above the system noise level out to about 6 Hz. Although the details of the roll-off for the experimental data are mostly hidden by the noise, there is some indication, particularly for 1 March 1991/Run No. 7, that the roll-

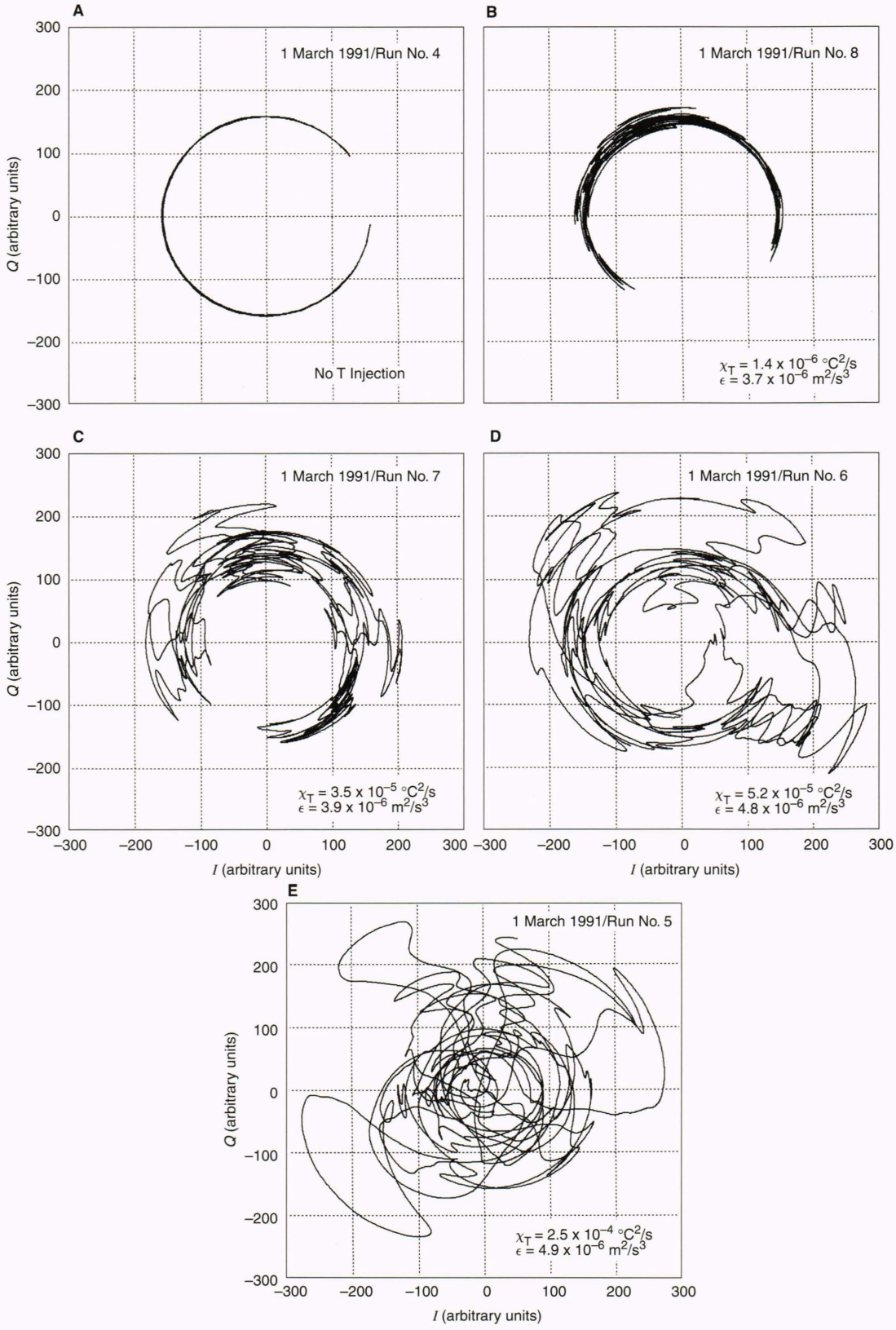

Figure 9. Phasor trajectories of the complex photocurrent $C(t)$ defined in Equation 18. The horizontal and vertical axes are, respectively, the in-phase (I) and quadrature (Q) components of the demodulated photocurrent. The trajectories are shown over the first half-second for the runs (1 March 1991) at 9.8 cm/s with the grid at $x/M = 15$. The sequence (a) through (e) corresponds to increasing values of the dissipation rate of temperature variance χ_T and the kinetic energy dissipation rate ϵ.

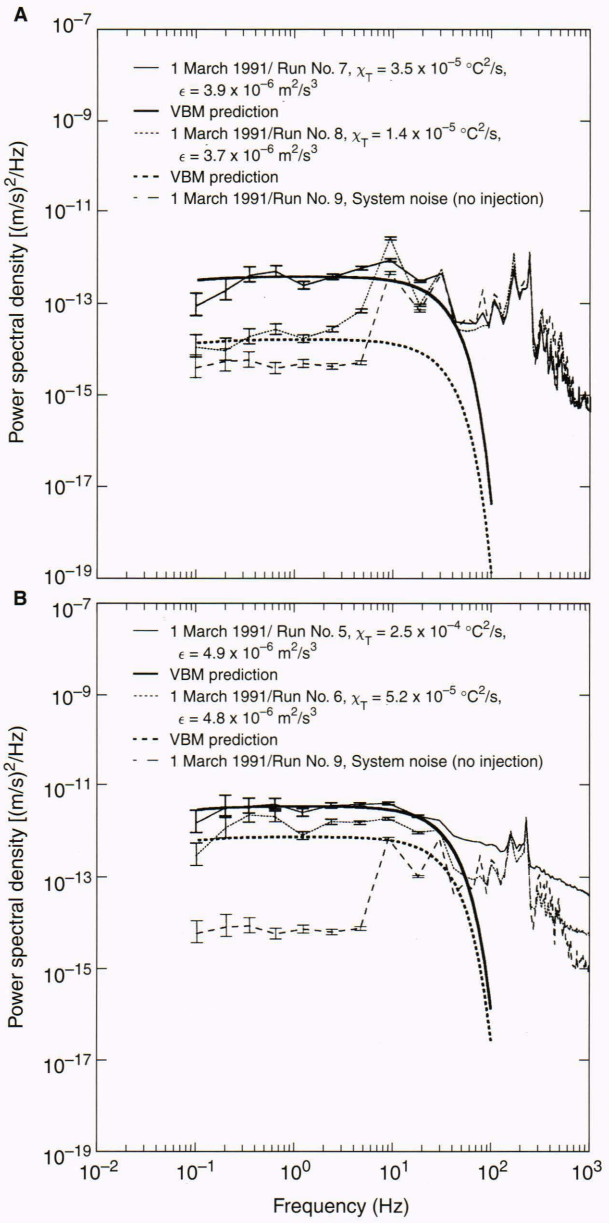

Figure 10. Comparisons between the model predictions of Vasholz, Baker, and Mack (VBM) and the experimentally derived equivalent velocity spectra. **A.** Results for the weakest refractive conditions of 1 March 1991. **B.** Results for the strongest refractive conditions of 1 March 1991. (ϵ = kinetic energy dissipation rate, χ_T = temperature dissipation rate.)

off is consistent with the model prediction (solid curve). The two strongest refractive runs are shown in Figure 10B. The highest injection run shows excellent agreement with the model prediction from the lowest frequency to about 30 Hz. Beyond 30 Hz, the model shows a roll-off, whereas the experimental results reveal additional energy at higher frequencies. This additional effect is caused by the amplitude variations discussed for the strongest refractive conditions and includes effects not modeled under the simplifying assumptions of the basic model. A detailed treatment of this additional effect at high frequency is beyond the scope of this article and will be left to a future discussion.

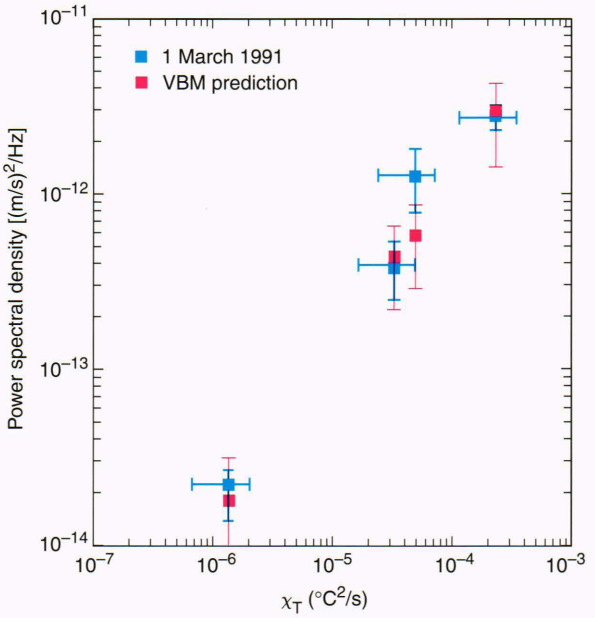

Figure 11. Comparison between the model predictions of Equation 8 and the experimentally derived results in the 0.15- to 3.0-Hz frequency range as a function of the dissipation rate of temperature variance χ_T. For these runs, speed U = 9.8 cm/s, location x/M = 15, distance L = 88 cm, and the kinetic energy dissipation rate ϵ ranged from 3.7×10^{-6} to 4.9×10^{-6} m^2/s^3; VBM = Vasholz, Baker, and Mack.

We can summarize the comparison with the model prediction for this experimental sequence by comparing the average spectral levels of both theory and experiment over the low-frequency spectral regime (0.15 to 3.0 Hz), where the signals are well above the noise. These spectral levels are plotted as a function of χ_T in Figure 11. Good agreement is apparent for each experiment. Further, the ϵ values are constant enough during this sequence (ranging from 3.7×10^{-6} to 4.9×10^{-6} m^2/s^3) to reflect the linear dependence on χ_T predicted by the model.

Another experimental sequence was conducted to achieve lower turbulence levels and lower refractive conditions. For this sequence, the grid was moved to a distance 500 cm upstream of the laser beam (x/M = 50, speed U = 11 cm/s). At an injection rate of 10 gpm, the χ_T value was about an order of magnitude lower than the highest injection run discussed in Figure 10B. The turbulence level was also about an order of magnitude lower. These experiments were conducted overnight (with building machinery turned off) to minimize the effects of vibration and hence better compare the experimentally determined spectral roll-off with that predicted by the VBM model. First, consider the background temperature and velocity ground truth measurements taken during this run and shown in Figure 12. Also shown are the Pao velocity spectrum based on the measured ϵ value and the Batchelor temperature spectrum based on the measured χ_T and ϵ values. Note that the temperature spectrum is significantly attenuated between 20 and 50 Hz because of the thermal diffusion for structures over these scales (wavelengths of 0.55 to 0.22 cm for U = 11cm/s). Although there is some difference between the measured temperature spectrum and the Batchelor spectrum at the

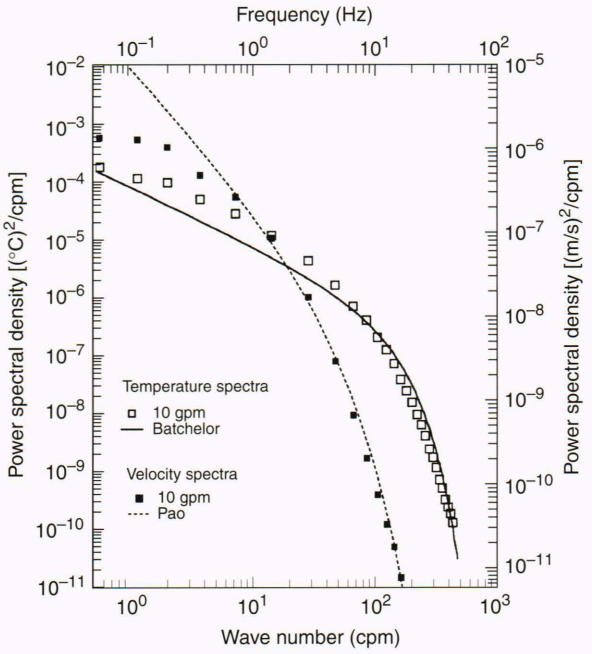

Figure 12. Comparison between measured results and universal spectra for the special low-noise experimental run. These results correspond to the results shown in Figure 13. (cpm = cycles per meter).

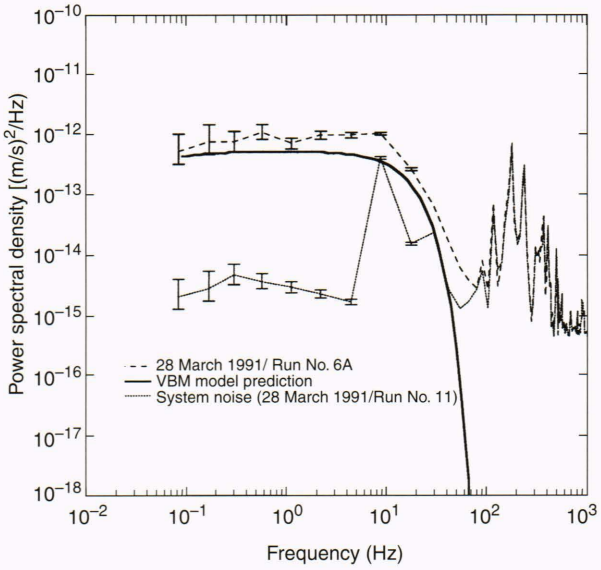

Figure 13. Comparison between the model predictions of Vasholz, Baker, and Mack (VBM) and the experimentally derived equivalent velocity spectra for the refractive condition of 28 March 1991/Run No. 6A (dissipation rate of temperature variance $\chi_T = 1.3 \times 10^{-5}$ °C²/s, kinetic energy dissipation rate $\epsilon = 3.8 \times 10^{-7}$ m²/s³, speed $U = 11$ cm/s).

low-frequency range (about a factor of 2), the higher-frequency roll-off regime shows reasonable agreement. Note that any difference between the temperature spectrum and Batchelor spectrum should translate into differences between the experimental optical results and the VBM model predictions, since the model assumes a Batchelor temperature spectrum.

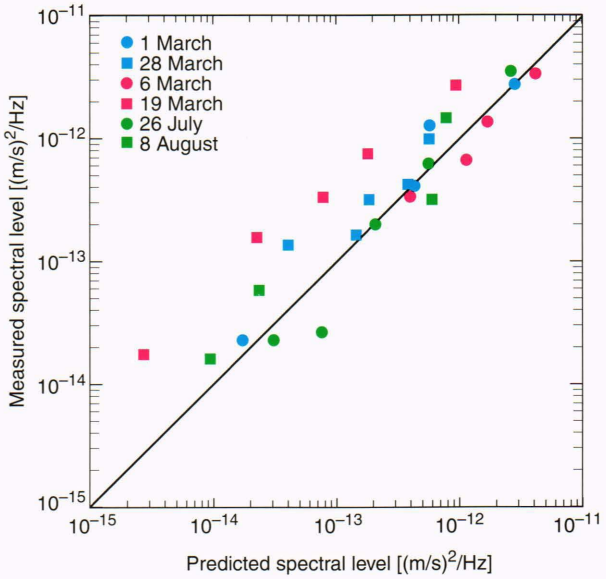

Figure 14. Comparison of measured and predicted equivalent velocity spectral levels in the 0.15- to 3.0-Hz regime for all experimental runs.

To compare the roll-off region of the equivalent velocity spectrum from the optical data with that predicted by the VBM model, we plotted the spectrum for the highest injection run of 28 March 1991, the noise curve, and the model prediction as presented in Figure 13. Since the signal curve includes signal plus noise, we have subtracted the values of the noise from the signal curve* to compensate partially for the underlying noise level—particularly in the roll-off regime. The theoretical prediction is slightly lower than the experimental data points (but within a factor of 2, and consistent with the underprediction of the Batchelor model curve of Fig. 12 compared with the measured temperature spectrum) below 10 Hz, but this run clearly shows that the predicted roll-off is in reasonable agreement with the experimental roll-off out to about 40 or 50 Hz, where the data fall into the noise.

The previous two sample runs are representative of the results for the full range of experimental conditions. For each of the run conditions, the spectral level for the equivalent velocity spectra obtained for the optical data have been computed over the frequency range of 0.15 to 3 Hz. The remaining experimental data sets obtained at mean speeds of about 5 and 15 cm/s and at downstream distances from the injection grid of $x/M = 15$ and 50 were similarly analyzed. The experimental spectral values are compared with the model predictions (again the average between 0.15 to 3 Hz) for all twenty-eight experiments in Figure 14. For an exact agreement between experiment and model, the points should lie on the 45° line also shown. Any bias in the model should show up as an offset of the prediction to the right or left of the straight line. Although there are a few more data points to the left, indicating slightly low model predictions, no significant

*The noise was subtracted only if the signal plus noise values exceeded the noise curve by a factor of 1.5.

bias exists between experiment and model over the 0.15- to 3-Hz regime for this analysis. Hence, the model has been validated over the range of conditions realized in our experiment.

General Remarks

The theoretical development and the detailed laboratory validation have provided a unique view of the effects of turbulence and refractive structure on optical phase. Progress has been made because of the ability to combine both theory and experimentation across several disciplines that include electromagnetism, optics, laser-Doppler velocimetry, interferometry, oceanography, turbulence, and scalar microstructure. We developed a versatile experimental facility that includes a low-turbulence recirculating flow channel and sensitive optical and turbulence measurements. The experiments have validated our model over a wide range of parameters (the turbulence and temperature microstructure levels overlap the relevant oceanographic levels, and the mean speeds approximate typical ocean currents) and have also suggested an increased complexity over a parameter range where the model assumptions are no longer valid. The validation for one part of the model has been associated with a single scalar, namely, temperature. The addition of salinity will provide another degree of complexity and experimental difficulty, since the smallest scales of salinity will be a factor of 10 smaller than those of temperature. Future challenges await with our planned experiments that will combine both temperature and salinity to represent the full complexity of the ocean density field.

REFERENCES

1. Abramovici, A., Althouse, W. E., Drever, R. W. P., Gursel, Y., Kawamura, S., et al., "LIGO: The Laser Interferometer Gravitational-Wave Observatory," *Science* **256**, 325-333 (17 April 1992).
2. George, W. K., and Lumley, J. L, "The Laser-Doppler Velocimeter and its Application to the Measurement of Turbulence," *J. Fluid Mech.* **60**, 321-362 (1973).
3. Vasholz, D. P., Baker, M. A., and Mack, S. A., *Optical Phase Fluctuations from Scalar Microstructure*, JHU/APL STD-R-1665 (1988).
4. Batchelor, G. K., "Small-Scale Variation of Convected Quantities like Temperature in Turbulent Fluid, Part 1. General Discussion and the Case of Small Conductivity," *J. Fluid Mech.* **5**, 113-133 (1959).
5. Pao, Y. H., "Structure of Turbulent Velocity and Scalar Fields at Large Wavenumbers," *Phys. Fluids* **8**, 1063-1075 (1965).
6. Nasmyth, P., *Ocean Turbulence*, Ph. D. dissertation, Institute of Oceanography, University of British Columbia (1970).
7. Gibson, C. H., "Fine Structure of Scalar Fields Mixed by Turbulence. II Spectral Theory," *Phys. Fluids* **11**, 2316-2327 (1968).
8. Gibson, C. H., Lyon, R. R., and Hirschsohn, I., "Reaction Product Fluctuations in a Sphere Wake," *AIAA J.* **8**, 1859-1863 (1970).
9. Abramowitz, M., and Stegun, I. A. (eds.), *Handbook of Mathematical Functions*, U.S. Dept. of Commerce, National Bureau of Standards Applied Mathematics Series, **55** (1966).
10. Perry, A. E., and Morrison, G. L., "Static and Dynamic Calibration of Constant Temperature Hot-Wire Systems," *J. Fluid Mech.* **47**, 765-777 (1971).
11. Hinze, J. O., *Turbulence*, McGraw-Hill, Inc., New York (1975).

ACKNOWLEDGMENTS: The work described in this article benefited greatly from the optical design efforts of Bernie Hochheimer, the flow system expertise of Joe Hopkins, and the software support supplied by Mel Hennessey. This work has been supported by the Office of Naval Research under SPAWAR Contract N00039-91-C-0001. A Stuart Janney Fellowship helped support the preparation of this manuscript.

THE AUTHORS

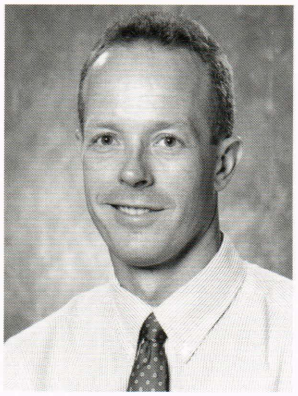

MARK A. BAKER received a Ph.D. in oceanography from the Scripps Institution of Oceanography, University of California, San Diego, in 1985. He joined APL in 1985 and is a member of the Principal Professional Staff and the Submarine Technology Department's Hydrodynamics Group (STH). Dr. Baker's main research interests are the statistics of small-scale mixing in the ocean and experiments on turbulent flow fields in the laboratory. Dr. Baker is the Supervisor of the STH Hydrodynamics Research and Calibration Laboratories. He is the Project leader for the SSBN Security Program's Hydrodynamics Project. In October 1990, Dr. Baker participated in an oceanographic study aboard a Soviet research vessel on the influence of islands on the equatorial undercurrent in the western Pacific. He is a member of the American Meteorological Society, American Geophysical Union, Oceanography Society, IEEE Oceanic Engineering Society, Pi Mu Epsilon, and Sigma Pi Sigma.

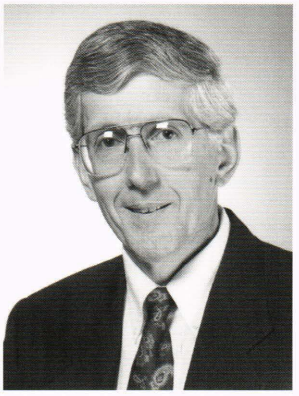

STEPHEN A. MACK received a B.S. in physics from St. Francis College in 1965 and an M.S. and Ph.D. (1967, 1971) in physics from Lehigh University. He was a postdoctoral fellow from 1971 to 1973 at the Department of Physics and Materials Research Department of the University of Illinois. Dr. Mack joined APL in 1973 and currently works in the Submarine Technology Department. He is interested in research on ocean small-scale mixing processes and has used both vertical profiling instruments and towed chain instruments to examine the relationship between ocean mixing and larger-scale ocean processes. He is a member of the Principal Professional Staff and Section Supervior of the Applied Sciences Section of the Hydrodynamics Group. Dr. Mack has served on several Navy committees concerning oceanographic issues related to Navy needs.

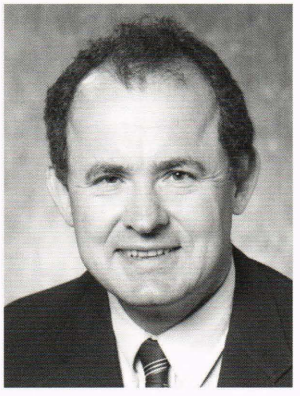

DAVID P. VASHOLZ received a B.S. in mathematics and physics from Valparaiso University in 1965 and a Ph.D. in theoretical physics in 1970 from the University of Wisconsin in Madison. He was a postdoctoral fellow and research associate from 1971 to 1974 at the Universities of Arizona and Florida. After serving as a research physicist at the Naval Coastal Systems Center in Panama City, Florida, he joined APL in 1978. He has published in a variety of areas, including elementary particle physics, quantum theory, acoustics, optics, and oceanography. He is a member of the Principal Professional Staff and is on the Technical Staff of the Hydrodynamics Group.